I&EC research
Industrial & Engineering Chemistry Research

Article

Cite This: Ind. Eng. Chem. Res. 2017, 56, 13206-13218

pubs.acs.org/IECR

CO_2 Hydrogenation over Pt-Containing UiO-67 Zr-MOFs—The Base Case

Emil Sebastian Gutterød,[†] Sigurd Øien-Ødegaard,[†] Koen Bossers,[†,‡] Anne-Eva Nieuwelink,[†,‡] Maela Manzoli,[§,#] Luca Braglia,[§,∥] Andrea Lazzarini,[†] Elisa Borfecchia,[§] Sajjad Ahmadigoltapeh,[†] Boris Bouchevreau,[†] Bjørn Tore Lønstad-Bleken,[†] Reynald Henry,[†] Carlo Lamberti,[§,∥] Silvia Bordiga,[†,§] Bert M. Weckhuysen,[‡] Karl Petter Lillerud,[†] and Unni Olsbye*[,†]

[†]Centre for Materials Science and Nanotechnology, Department of Chemistry, University of Oslo, Sem Saelandsvei 26, N-0315 Oslo, Norway

[‡]Inorganic Chemistry and Catalysis Group, Debye Institute for Nanomaterials Science, Utrecht University, Universiteitsweg 99, 3584 CG Utrecht, The Netherlands

[§]Department of Chemistry, NIS Interdepartmental Centre and INSRM reference centre, University of Turin, via Quarello 15A, I-10135 Turin, Italy

[∥]IRC "Smart Materials", Southern Federal University, Zorge Street 5, 344090 Rostov-on-Don, Russia

Supporting Information

ABSTRACT: CO_2 hydrogenation was carried out over Pt-containing UiO-67 Zr-MOFs at T = 220−280 °C and ambient pressure, with H_2/CO_2 = 0.2−9 and contact times, τ = 0.004−0.01 $g_{cat}\cdot min\cdot mL^{-1}$. The catalysts were characterized by XRD, N_2 adsorption, FESEM, TEM and HRTEM, Pt L_3-edge XANES and EXAFS, dissolution-NMR, CO chemisorption, IR spectroscopy, and TGA. A positive correlation was observed between the degree of Pt reduction and CO_2 conversion. Contact time variation experiments showed that CO is a primary product of reaction, while CH_4 is a secondary product. Testing of catalyst crystals with 0.15 and 2.0 μm crystal size, respectively, revealed no influence of diffusion on the reaction rate. Comparison to a conventional Pt/SiO_2 catalyst showed very similar activation energy, with E_{app} = 50 ± 3 $kJ\cdot mol^{-1}$. However, the turnover frequency over Pt/SiO_2 was significantly lower, and Pt/SiO_2 did not yield methane as a product. The Pt-containing UiO-67 Zr-MOF catalyst showed stable activity during 60 h of testing.

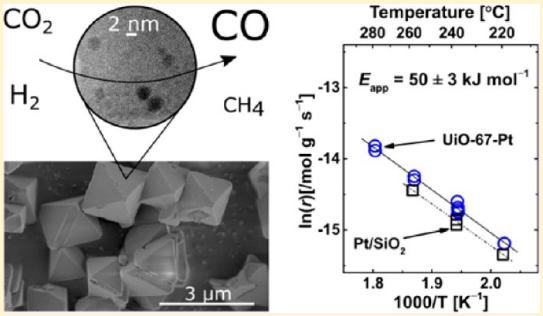

1. INTRODUCTION

CO_2 is a key contributor to global warming and ocean acidification, and its recycling to valuable products by chemical conversion is an attractive research target. Thermodynamically, CO_2 is the most stable molecular product of carbon combustion, and its valorization is energy demanding.[1] Therefore, to activate CO_2, a high energy-density carrying agent is required, in the form of photons, electrons, or chemical energy. H_2 has a high gravimetric energy density of 143 $MJ\cdot kg^{-1}$, making it a suitable candidate for the chemical conversion of CO_2.[2] Some key reactions for CO_2 and H_2 conversion are given below.

The reverse water gas shift reaction (RWGS):

$$CO_2 + H_2 \rightarrow CO + H_2O \quad (1)$$

$$\Delta H_{298K} = 41.2\ kJ\ mol^{-1}$$

$$\Delta G_{298K} = 28.6\ kJ\ mol^{-1}$$

Methanol formation:

$$CO_2 + 3H_2 \rightarrow CH_3OH + H_2O \quad (2)$$

$$\Delta H_{298K} = -49.5\ kJ\ mol^{-1}$$

$$\Delta G_{298K} = 3.8\ kJ\ mol^{-1}$$

CO_2 methanation:

$$CO_2 + 4H_2 \rightarrow CH_4 + 2H_2O \quad (3)$$

$$\Delta H_{298K} = -252.9\ kJ\ mol^{-1}$$

$$\Delta G_{298K} = -113.5\ kJ\ mol^{-1}$$

The methanation reaction is thermodynamically favored, but a catalyst is needed to overcome the kinetic limitations. Ni-containing catalysts are used for the reverse reaction at high

Special Issue: Tapio Salmi Festschrift

Received: April 15, 2017
Revised: July 15, 2017
Accepted: July 18, 2017
Published: July 18, 2017

DOI: 10.1021/acs.iecr.7b01457
Ind. Eng. Chem. Res. 2017, 56, 13206−13218

temperatures and are also active for reaction 3.[3−6] However, deactivation of Ni-based catalysts at low temperatures, by formation of mobile nickel subcarbonyls, is a major obstacle. Catalysts containing noble metals like Ru, Pd, or Pt are more stable under these conditions and are therefore more active for CO_2 methanation.[3] In the current study, focus is set on Pt-based catalysts.

Previous studies of Pt-based CO_2 catalysts include a classical contribution from Román-Martínez et al.[7] They studied Pt/C and Pt-M/C (M = Mg, Ca) as CO_2 hydrogenation catalysts and reported a negative correlation between Pt particle size and turnover frequency for the RWGS reaction (eq 1) over Pt/C at 300−400 °C. Later, Iglesia and Wei[8] studied the reverse methanation reaction (eq 3), i.e., methane reforming to synthesis gas (CO, CO_2, and H_2), over supported Pt catalysts (γ-Al_2O_3, ZrO_2, ZrO_2−CeO_2 supports) at 550−800 °C and 0.1−1.0 bar total pressure. They reported that C−H bond breaking was the rate-determining step of methane reforming and that the turnover frequency (TOF) of methane activation increased with a decreasing Pt particle size, suggesting that C−H bond breaking is a structure-sensitive reaction, where the low-coordinated sites are more active than sites in low-index planes. Together, these two studies suggest that stabilization of small Pt particles is an attractive target in the development of catalysts for the CO_2 hydrogenation reaction, aiming at syngas or methane production, and led to the selection of a Zr-MOF support in the present study.

Metal organic frameworks (MOFs) are a class of crystalline, porous materials in which inorganic clusters are connected by organic linker molecules.[9,10] By adjusting the chemical nature of the clusters and the linker molecules, different architectures can be obtained from 2D to 3D porous networks, with a wide variety of pore sizes, from the microporous to the mesoporous region.[9] Furthermore, the linkers can be functionalized with different chemical groups, e.g., to enhance gas adsorption,[11−13] or to mimic ligands in organometallic complexes and thereby stabilizing homogeneous organometallic complex catalysts in a solid matrix.[10,14,15] However, most MOF materials suffer from low thermal, chemical, and mechanical stability.[16]

UiO-67 is a microporous MOF belonging to the UiO Zr-MOF series and is built from $Zr_6O_4(OH)_4$ clusters connected by 1,1′-biphenyl-4,4′-dicarboxylic acid (bpdc) linker molecules.[16] UiO-67 has been reported to be kinetically stable up to 450 °C in a N_2 atmosphere, after which it starts to break down due to cleavage of the C−C bond between the phenyl ring and the carboxylic acid group.[16] The material has both octahedral and tetrahedral cavities with sizes of 23 and 11.5 Å, respectively. UiO-67 has a remarkably high theoretical BET surface area of 2800 $m^2 \cdot g^{-1}$. To incorporate metal species for catalysis, different functionalized linkers have been introduced into the network of UiO-67 together with bpdc. A variety of methods have been reported, such as premade linker synthesis (PMLS), postsynthetic functionalization (PSF), and one pot synthesis (OPS).[10,14,15] These methods vary by the stage at which the metal species is introduced in the framework. OPS is the least sophisticated method, in which all precursors are mixed together as noncoordinated, individual components in a solvent to synthesize a modified UiO-67 framework. For PMLS, the metal species is first coordinated to a functionalized linker molecule and then mixed with the other components during UiO-67 synthesis. Finally, PSF involves the grafting of the metal species to a chelating linker after the synthesis of UiO-67.

Over the past few years, several studies have explored the UiO-series of Zr-MOFs for catalytic applications.[17] Much due to the high complexity and tunability of MOFs, catalysis may occur at various locations, such as at the Zr cluster,[18,19] metalated linker,[14,20] or encapsulated metal particles.[21−26] Here, we focus on catalysis over UiO-MOFs containing $PtCl_x$ entities and Pt nanoparticles (NPs).

To the best of our knowledge, the first study of Pt-containing Zr-MOFs was reported by Guo et al.[23] in 2014. Pt NPs were formed inside the cavities of UiO-66-NH_2 during reduction (10% H_2 in Ar at 200 °C for 1 h) of K_2PtCl_4 impregnated MOF and tested for liquid phase hydrogenation of cinnamaldehyde. After 42 h of reaction, a conversion of 86% with 88% selectivity toward cinnamyl alcohol was achieved. When the reaction was performed over UiO-66-NH_2 with Pt NPs located on the external surface of the MOF, a lower selectivity (72%) was observed.

In 2015, Choi et al.[24] encapsulated Pt NPs (2.5 nm) inside pristine and functionalized UiO-66 (linkers functionalized with $-SO_3H$, $-NH_3^+$, $-SO_3Na$, and $-NH_2$) and tested it catalytically for the conversion of methylcyclopentane (MCP). All the samples tested had their crystallinity, morphology, and chemical functionalities intact after 8 h of reaction. The nature and combination of the linker's functional groups was shown to greatly influence the catalytic pathway for MCP conversion, reactivity, and selectivity.

Very recently, Hester et al.[25] investigated UiO-67-Pt and UiO-67 with encapsulated Pt nanoparticles (both produced through the PMLS method) as catalysts for the oxidation of 5-hydromethylfurfural (HMF) to 2,5-furandicarboxylic acid (FDCA), and for reduction to 2,5-dimetylfuran. The catalytic reactions were performed at 60 °C in an autoclave reactor with 20 mL of aqueous solution of HMF, pressurized to 20 bar using O_2 and H_2 for the oxidation and reduction reaction, respectively. Although formation of FDCA was only observed in the presence of UiO-67-Pt-NPs, consumption of HMF was also observed over UiO-67 and UiO-67-Pt. Hester et al. argued that the consumption over the UiO-67 MOFs without Pt NPs was due to adsorption of HMF on their hydrophobic and porous structures. Under reducing conditions, adsorption of HMF by UiO-67 was again observed; however, 2,5-dimetylfuran was formed over both Pt-containing MOFs. The activity of UiO-67-Pt was suggested as due to *in situ* reduction of Pt since 2,5-dimetylfuran was only observed after about 30 min under reaction conditions.

Zhuang et al.[26] compared the activity of pristine UiO-67 for the CO oxidation with samples functionalized with 5-(4′-carboxyphenyl)picolinic acid or 2-aminobiphenyl-4-4′-dicarboxylic acid, all containing highly dispersed Pt NPs (PSF-type method). Larger Pt NPs were identified for UiO-67-Pt as compared to the two functionalized samples (4.5 nm versus 2.5 nm), suggesting that the functional group of the organic linker molecule and the pore size of the MOF influence the Pt particle size. The highest activity toward CO oxidation was observed for the 5-(4′-carboxyphenyl)picolinic acid functionalized sample, followed by pristine UiO-67-Pt, while the 2-aminobiphenyl-4-4′-dicarboxylic acid functionalized sample gave the lowest activity. Based on DFT calculations, it was argued that the higher activity of the 5-(4′-carboxyphenyl)picolinic acid functionalized sample was related to generation of a conjugate system between the pyridine N atom and the phenyl group, effectively adjusting the electronic structure of the MOF. In combination, the catalytic

DOI: 10.1021/acs.iecr.7b01457
Ind. Eng. Chem. Res. 2017, 56, 13206−13218

Table 1. Sample Characterization

sample	S_g (m^2 g^{-1})	V_m (cm^3 g^{-1})	crystal size (μm)	bipyridine loading (%)	Pt/Zr ratio (%)	Pt dispersion (%)
UiO-67-Pt-PMLS	2442	0.96	2.5			
UiO-67-bipy(M)	2683	1.03	2.5	5.5		
UiO-67-Pt-PSF(M)	2633	1.05	2.6	4.2		
UiO-67-bipy(N)	2460	1.00	2	4.5		
UiO-67-Pt-PSF(N)	2392	0.97	2		2.6 ± 0.3	5
UiO-67-Pt-PSF(N), pellets	2305	0.94	2			
UiO-67-Pt−PSF(N), tested for 52 h	2343	1.01	2			8
UiO-67-Pt-PSF(SA)	1882	1.24	0.15	4	1.8 ± 0.1	5
5% Pt/SiO_2 (Escat 2351, abcr)[a]	400					10

[a]Pt content and specific surface area values obtained from provider.

properties were concluded as dependent on both the size of the Pt NPs and the nature of the support.

In the present study, UiO-67-Pt was prepared by the PMLS and PSF method and studied as a catalyst for the CO_2 hydrogenation reaction in the gas phase. The aim of the study was to elucidate two essential features of the catalysts: their stability during catalytic operation and the potential influence of the MOF lattice on the target reaction.

2. EXPERIMENTAL SECTION

2.1. Material Synthesis. All chemicals were used as received. $ZrCl_4$ (Sigma-Aldrich) must be dry and of high purity for successful synthesis. $PtCl_2$(2,2′-bipyridine-5,5′-dicarboxylic acid) was synthesized using a previously reported method.[10] One batch of UiO-67-Pt by PMLS and three batches of UiO-67-Pt by PSF were prepared. One of the PSF batches was prepared on a small scale, labeled UiO-67-Pt-PSF(M), while two were prepared on a larger scale (2.5 L starting solution), labeled UiO-67-Pt-PSF(N) and UiO-67-Pt-PSF(SA). The detailed synthesis procedures are described in the Supporting Information.

In brief, samples of UiO-67-Pt were prepared by heating solutions of $ZrCl_4$, benzoic acid, H_2O, H_2bpdc, and either $PtCl_2$(H_2bpydc) (PMLS) or H_2bpydc (PSF) in dimethylformamide (DMF) at elevated temperatures for several days. The obtained powder (yellow in the PMLS sample, and white in the PSF samples) was first washed in hot DMF and then thoroughly washed in either tetrahydrofuran (THF) or acetone, then dried at 150−200 °C.

The samples prepared using H_2bpydc were functionalized with Pt by submerging the MOF and K_2PtCl_4 in DMF and heating the solution overnight at 100 °C. The obtained yellow powder was washed twice in DMF (100 °C) and then several times in either THF or acetone and then dried at 150 °C.

2.2. Material Characterization. Powder X-ray diffraction (XRD) patterns of the MOF samples before and after Pt-functionalization, mechanical stress, activation, and operation were obtained using a Bruker D8 Discover diffractometer with a Cu Kα source and Lynx Eye silicon detector.

The specific surface area and pore volume of the samples were determined from N_2 adsorption isotherms at −196 °C, performed with a BELSORP mini-II instrument. Prior to the measurement, the samples were heated under a vacuum at 80 °C for 1 h and at 150 °C for 2 h. A Hitachi SU8230 field emission scanning electron microscope (FESEM) with an XFlash 6|10 energy-dispersive X-ray (EDX) detector was utilized to assess the microstructure and the Pt/Zr ratio of the catalysts.

CO chemisorption measurements were performed using a pulse method.[27,28] Prior to the measurements, the samples were heated to 350 °C in a flow of 10% H_2 in Ar (50 mL·min^{-1}), followed by a 2 h isotherm where the last hour was in a flow of Ar. The samples were subsequently cooled rapidly to room temperature in a flow of Ar. Several CO pulses were introduced to a stream of Ar flowing through a reactor containing sample at room temperature and ambient pressure. The amount of CO leaving the reactor was determined using a mass spectrometer (MS; Pfeiffer Vacuum Omnistar QM200). Pulsing was continued until saturation. The MS response at saturation was used for calibration.

FT-IR spectra were collected on a Bruker Vertex80 instrument equipped with a MCT detector. Prior to the measurements, the samples were pressed into pellets without any dilution and heated to 150 °C under a vacuum. Then, 50 mbar of H_2 was dosed to the pellets, in order to remove the oxide layer present on the surface of the Pt nanoparticles of the catalysts. Then, 40 mbar of CO was dosed at room temperature as a probe to investigate the metal nanoparticles present on the catalysts; 32 spectra with a resolution of 2 cm^{-1} were averaged for each single acquisition during CO desorption under a dynamic vacuum.

Solution state nuclear magnetic resonance (NMR) was utilized to estimate the amount of bipyridine linkers in the MOF samples. NMR samples were prepared by dissolving 20 mg of MOF in 1 mL of a 1 M solution of NaOH in D_2O and leaving the mixture overnight to separate the solid inorganic phase from the aqueous solution by decantation. A ^1H NMR spectrum was acquired from 0.6 mL of the remaining solution.

Thermogravimetric Analysis−Differential Scanning Calorimetry (TGA-DSC) was used to elucidate the stability of different MOF samples. The samples were heated from 20 to 900 °C at a rate of 5 °C·min^{-1} under a flow of synthetic air (20 mL·min^{-1} N_2 and 5 mL·min^{-1} O_2).

Transmission electron microscopy (TEM) and high resolution (HR) TEM images were obtained with a Jeol 3010-UHR microscope operating at 300 kV equipped with a LaB_6 filament and with an Oxford Inca Energy TEM 300 EDS X-ray analyzer from Oxford Link. Digital micrographs were acquired with an Ultrascan 1000 camera and processed with a Gatan digital micrograph. Before the experiments, the samples, in the form of powders, were milled in an agate mortar and deposited on a copper grid covered with a lacey carbon film. Histograms of the particle size distribution were obtained by considering 1545 nanoparticles, and the mean particle diameter (d_m) was calculated as $d_m = \sum d_i n_i / \sum n_i$, where n_i was the number of particles of diameter d_i. The counting was carried out on electron micrographs obtained starting from 150 000× instrumental magnification, where Pt particles well contrasted with respect to the UiO-67 framework were clearly detected.

2.3. Catalyst Testing. Catalytic testing was performed in a fixed bed flow setup with a straight quartz tubular reactor (6 mm

DOI: 10.1021/acs.iecr.7b01457
Ind. Eng. Chem. Res. 2017, 56, 13206−13218

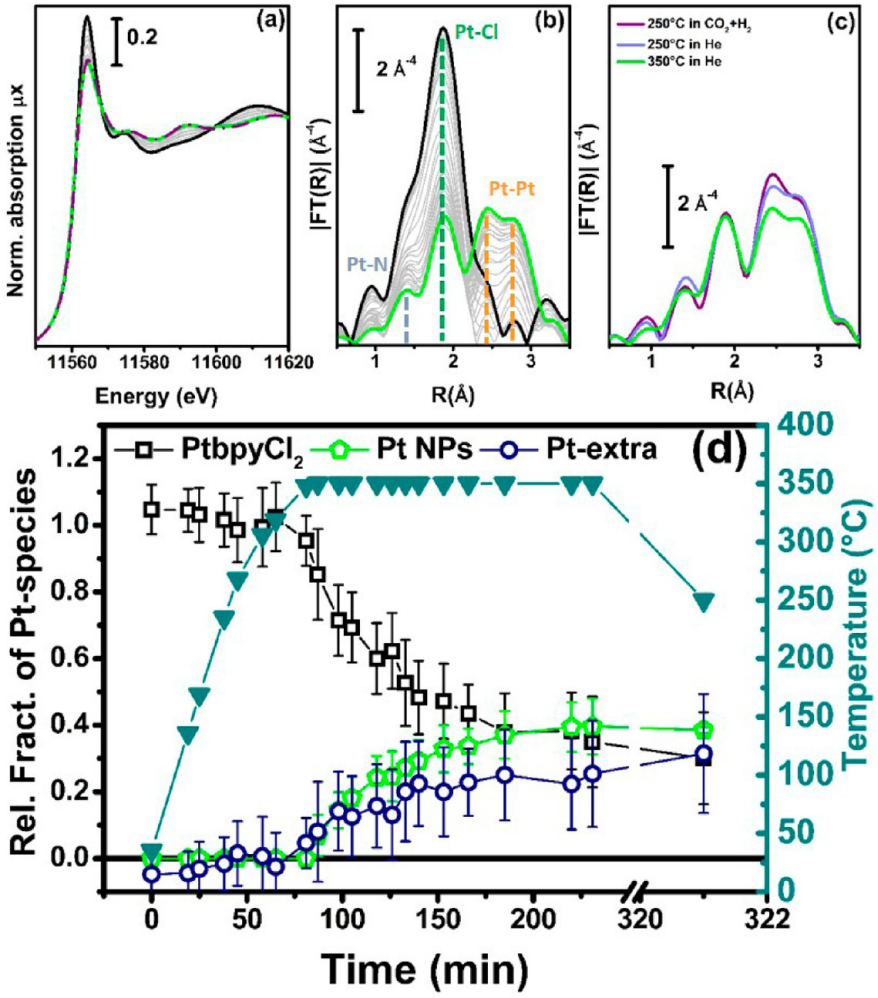

Figure 1. (a) Evolution of the Pt L_3-edge XANES spectra during in situ H_2-temperature-programmed reduction experiment of UiO-67-Pt-PSF(M) performed in 10% H_2/He flow in the temperature range 30−350 °C, followed by cooling in He to 250 °C and catalytic testing in H_2/CO_2/He = 6:1:3 flow at 250 °C. The XANES spectrum collected at 250 °C after 1.30 h of H_2/CO_2/He feed is reported as the dashed purple line. (b) As part a for the k^3-weighted, phase uncorrected, FT of the corresponding EXAFS data. Also highlighted with blue, green, and orange dashed lines are the typical positions of the Pt−N, Pt−Cl, and Pt−Pt contributions, respectively. (c) k^3-weighted, phase uncorrected, FT of the sample activated at 350 °C (green), cooled down to 250 °C in He (lilac), and treated in CO_2 and H_2 at 250 °C (purple). (d) Empty black, green, and blue symbols, left ordinate axis: fraction of the different Pt phases present in the sample, estimated from the N_{Pt-N}, N_{Pt-Cl}, and N_{Pt-Pt} coordination numbers obtained from the parametric refinement of the whole set of EXAFS data. In the right ordinate axis is reported the evolution of the sample temperature with time, highlighting the linear increase up to 350 °C in 65 min followed by a 2 h and 55 min isotherm, and finally 1.30 h under reaction conditions at 250 °C. Data obtained during pretreatment are reproduced from ref 32, data obtained under CO_2 hydrogenation conditions are new.

inner diameter), operated at ambient pressure. Dependent on the experimental aim, 0.1−0.2 g of catalyst (177−250 μm or 250−425 μm mesh) was loaded in the reactor and activated at 350 °C (1 h following ramp from room temperature) in a flow of 0, 3, or 10% H_2 in Ar (50 mL·min^{-1}). Subsequently, the catalyst was cooled under inert conditions (50 mL·min^{-1}) to 240 °C, then brought to steady-state performance at a H_2/CO_2 ratio of 6 and contact time (τ) of 0.01 g_{cat}·min·mL^{-1}, for at least 6 h before changing any parameters of operation. The respective steady-state conditions will be referred to as the *reference conditions*.

The influence of pCO_2 (0.08−0.40 bar), pH_2 (0.02−0.9 bar), T (220−280 °C), and τ (0.004−0.01 g_{cat}·min·mL^{-1}) on the catalytic activity was investigated by operating the catalyst under a given set of parameters in segments of 2 h. After a series of three to five segments of variable conditions, a segment at the reference conditions was included. In this manner, any changes in the activity with time on stream (TOS) could be monitored. Qualitative analysis of the effluent gas was performed during catalyst activation using a quadrupole mass spectrometer (Pfeiffer Vacuum Omnistar QM200). Furthermore, the volumetric concentrations of products and reactants were quantified using a two-channel microgas chromatograph (μGC 3000A, Agilent), equipped with a molecular sieve column with Ar as the carrier gas and a TCD detector and a Plot U column with He as the carrier gas and a TCD detector.

3. RESULTS AND DISCUSSION

3.1. Catalyst Characterization. Characterization data for fresh, pressed and sieved, preactivated and tested catalysts are summarized in Table 1. More detailed analysis, considering XRD patterns, FESEM images, TEM and HRTEM images, and TG curves, is illustrated by the corresponding figures and graphs in section 3.3.

As a general comment on the data in Table 1, all materials had initial specific surface areas close to the theoretical value of 2800 $m^2 \cdot g^{-1}$ for UiO-67.[12] Furthermore, as will be seen in section 3.3,

DOI: 10.1021/acs.iecr.7b01457
Ind. Eng. Chem. Res. 2017, 56, 13206−13218

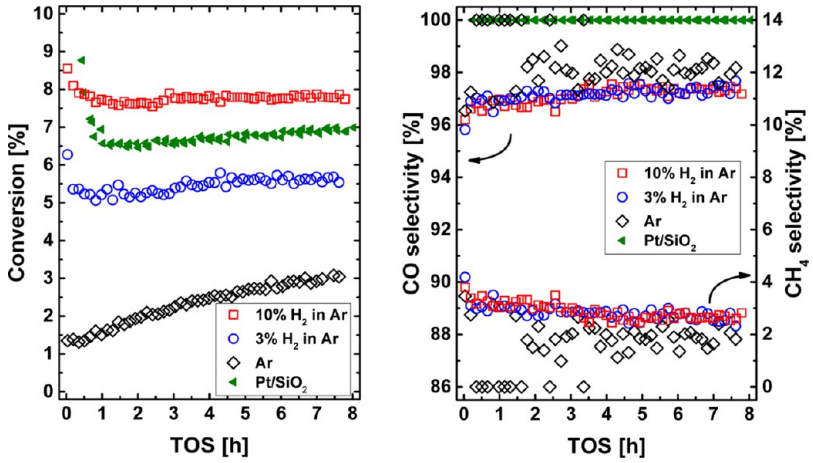

Figure 2. Left: Conversion (%) versus time on stream (hours, h) observed for UiO-67-Pt-PSF(M) under reference conditions after preactivation at 350 °C (1 h) in a flow of Ar with 0, 3, and 10% H_2 (50 mL·min^{-1} total flow). The respective CO and CH_4 selectivities are shown in the figure to the right. The conversion and CO selectivity observed for Pt/SiO_2 is marked with green tilted triangles.

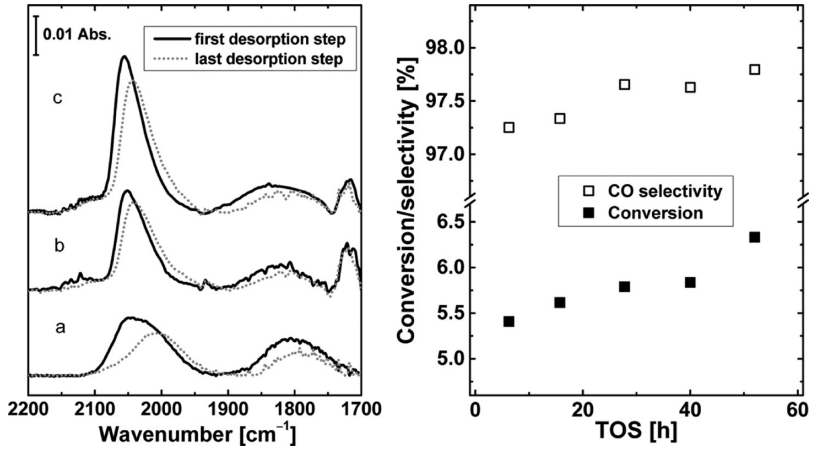

Figure 3. Left: FT-IR spectra of CO adsorbed on Pt nanoparticles supported on SiO_2 (a) and on UiO-67-Pt-PSF(N) after preactivation in 10% H_2/Ar (b) and after testing for the CO_2 hydrogenation reaction under 10−20 mL·min^{-1} flow of H_2/CO_2/Ar = 6:1:3 at temperatures in the range 220−280 °C for 52 h (c). The spectra are focused on the spectral region of CO vibrational modes and are shown after subtraction of the spectrum of the samples prior to CO adsorption. Right: Evolution of CO_2 conversion and CO selectivity over UiO-67-Pt-PSF(N) during time on stream. FT-IR spectra (b and c) correspond to 0 and 52 h on stream, respectively.

all samples were crystalline and contained only one crystalline phase. The crystal size and bipy content of all PMLS and PSF samples were similar, except for the crystal size of the UiO-67-Pt-PSF(SA) sample, which was an order of magnitude smaller than that of the other UiO-67-Pt-PSF and UiO-67-Pt-(PMLS) samples. The Pt/Zr ratio of the UiO-67-Pt-PSF(SA) sample was somewhat lower than that of UiO-67-Pt-PSF(N), resulting in an estimated Pt content of 1.2 and 1.5 wt % for the two samples, respectively. The Pt content was derived from the Pt/Zr ratios and the amount of defects estimated by TG of the supports (Figures S9 and S10).[29,30] The Pt dispersion of the samples after activation in 10% H_2/Ar at 350 °C was low (5−10%), suggesting either large Pt particle sizes or that a fraction of the Pt content is inaccessible for adsorption, e.g., due to incomplete reduction. By following the procedure described in ref 31, the theoretical dispersion of the Pt NPs of UiO-67-Pt can be estimated to 14%, assuming complete reduction and spherical shaped NPs (d = 2.6 nm (section 3.3.2)). However, as seen in section 3.2.1 and Figure 1, barely 40% of the Pt is in the form of NPs after the reduction; when the incomplete reduction of Pt is considered, the Pt dispersion of the UiO-67-Pt samples increases to about 13% and is in good agreement with the theoretical value. For the Pt/SiO_2 sample, the average Pt NP size can be estimated from the 10% dispersion to about 4 nm in diameter. This means that the samples were well suited for comparisons of catalytic performance and lattice stability.

3.2. Catalyst Testing. *3.2.1. Influence of Activation Atmosphere on Catalyst Activity.* Recently, our team reported an *in situ* XAS study[32] of the oxidation state and coordination of Pt in the UiO-67-Pt-PSF(M) sample studied here, during activation at 350 °C in pure He and in 10% H_2/He, respectively (Figure 1). The XAS data revealed that Pt−Pt bonds, indicating Pt metal cluster formation, were only formed in the H_2-containing feed. The fraction of Pt being associated with another Pt atom was around 40% and was approaching an asymptotic limit after 3 h of activation at 350 °C in 10% H_2/He. Under a pure He feed, the fraction of Pt atoms coordinated to Cl and N decreased during heating, starting at 280 °C. At 350 °C, only 60% of the Pt remained in the original (bipy)-$PtCl_2$ coordination. However, no Pt−Pt bond formation was observed, even after continued heating to 480 °C.[32]

DOI: 10.1021/acs.iecr.7b01457
Ind. Eng. Chem. Res. 2017, 56, 13206−13218

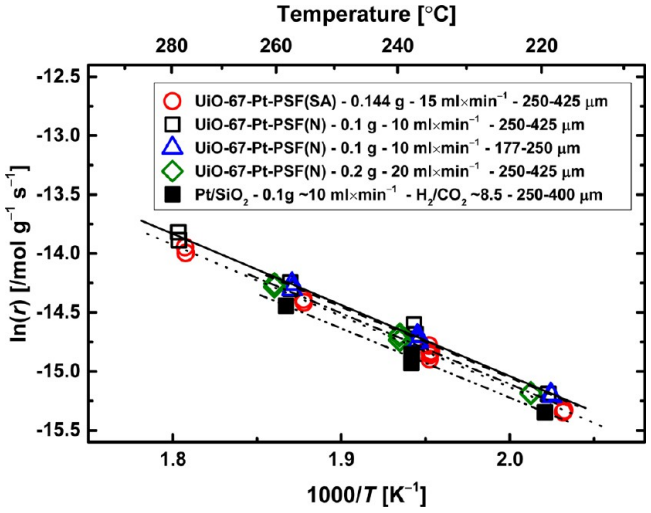

Figure 4. Arrhenius type plot of the rate of CO_2 conversion in the temperature range 220−280 °C, at pCO_2 = 0.1 bar, pH_2 = 0.6 bar, and τ = 0.01 g_{cat}·min·mL^{-1}. Test series of UiO-67-Pt-PSF(N) are marked with squares, triangles, and diamonds. The test of the small crystallite UiO-67-Pt-PSF(SA) sample is marked by circles, and the test of Pt/SiO_2 is marked by filled squares.

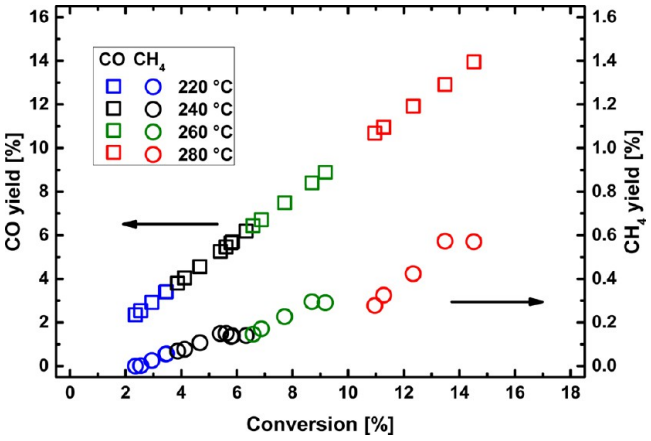

Figure 5. Yield (%) of CO (left axis) and CH_4 (right axis) versus CO_2 conversion (%) obtained over UiO-67-Pt-PSF(N) under a flow of H_2/CO_2/Ar = 6:1:3 and τ = 0.004−0.01 g_{cat}·min·mL^{-1}, in the temperature range 220−280 °C.

Recently, the Fourier transform of EXAFS data for the same material was monitored after activation in 10% H_2/He at 350 °C (green), further cooling to 250 °C in He (lilac) and subsequently 1.30 h in H_2/CO_2/He = 6:1:3 flow (Figure 1a). The three spectra look very similar; there is a difference in intensity in the 2−3 Å range between the spectra obtained at different temperatures; however, the difference is due to the Debye−Waller factor effect. To confirm this, a comparison was made of the XANES spectra, which are not influenced by the temperature, after the end of the temperature ramp and after interaction with H_2/CO_2, respectively. The two spectra are precisely overlapped, suggesting that the H_2/CO_2 feed did not induce significant changes to the material under the relatively short interaction period of this experiment.

In this study, the conversion and product distribution of a H_2/CO_2/Ar = 6:1:3 feed over UiO-67-Pt-PSF(M) at T = 240 °C and τ = 0.01 g_{cat}·min·mL^{-1} was measured directly after activation in flows of 0, 3, and 10% H_2/Ar for 1 h at 350 °C in the home lab, to

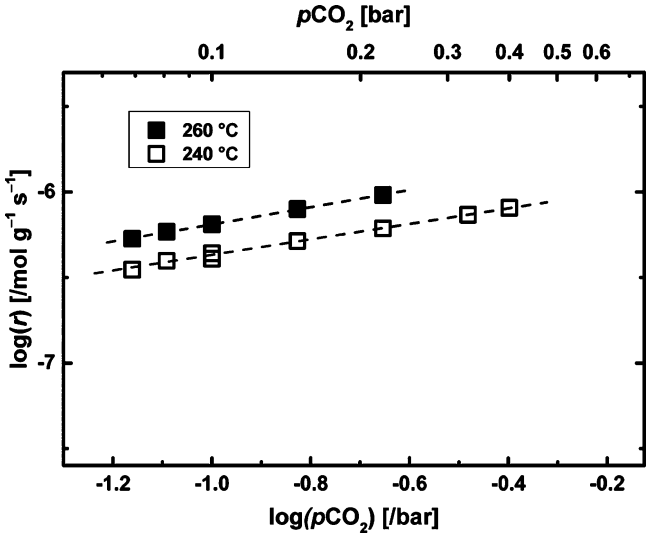

Figure 6. pCO_2 dependence of the CO rate of formation over UiO-67-Pt-PSF(SA) at 240 °C (open) and 260 °C (filled). pH_2 = 0.6 bar and τ = 0.01 g_{cat}·min·mL^{-1}.

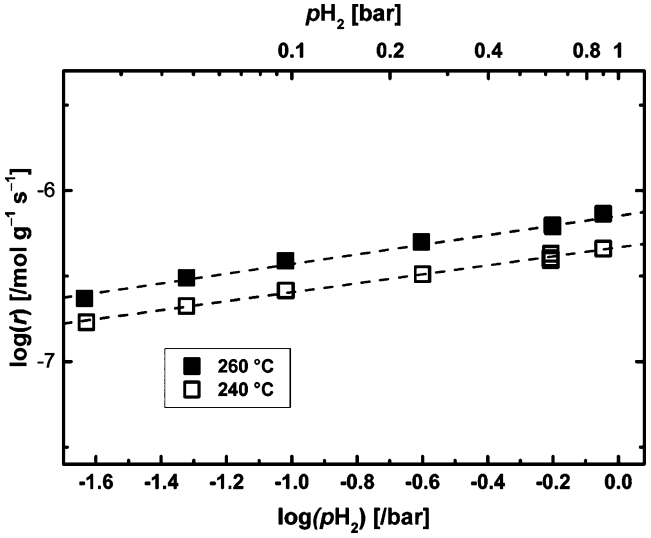

Figure 7. pH_2 dependence of the CO rate of formation over UiO-67-Pt-PSF(N) at 240 °C (open) and 260 °C (filled). pCO_2 = 0.1 bar and τ = 0.01 g_{cat}·min·mL^{-1}.

Table 2. Apparent Activation Energy of CO_2 Conversion over Various Samples of UiO-67-Pt-PSF and Pt/SiO_2, Estimated from the Arrhenius Plot in Figure 4

sample	E_{app} (kJ mol^{-1})
UiO-67-Pt-PSF(SA): 0.14 g, 15 mL min^{-1}, 250−425 µm	50 (±1.1)
UiO-67-Pt-PSF(N): 0.1 g, 10 mL min^{-1}, 250−425 µm	50 (±1.5)
UiO-67-Pt-PSF(N): 0.1 g, 10 mL·min^{-1}, 177−250 µm	50 (±1.3)
UiO-67-Pt-PSF(N): 0.1 g, 10 mL min^{-1}, 250−425 µm	50 (±1.1)
Pt/SiO_2: 0.1 g, ~10 mL min^{-1}, H_2/CO_2 ~ 8.5, 250−400 µm	49 (±2.6)

correctly reproduce the test conditions used during XAS measurements at the synchrotron. The results are shown in Figure 2. Activation performed in 0% H_2/Ar led to an initial conversion around 1.5% which increased gradually to 3% during the following 8 h on stream. When the H_2 content was increased to 3% during activation, a significantly higher initial conversion (5.5%) was achieved, however only a slight increase with TOS

DOI: 10.1021/acs.iecr.7b01457
Ind. Eng. Chem. Res. 2017, 56, 13206−13218

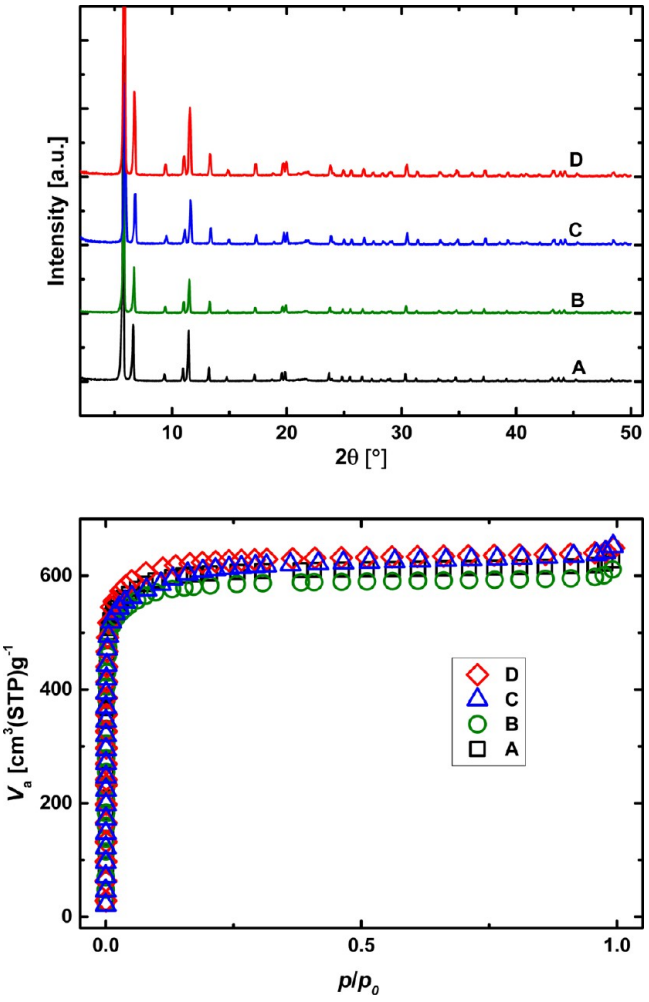

Figure 8. XRD patterns and N_2 adsorption isotherms of UiO-67-Pt-PSF(N) in the form of powder (A) and pellets (B, pressed at 0.5 tons) and after preactivation in 10% H_2/Ar followed by testing for the CO_2 hydrogenation reaction under a 10−20 mL·min^{-1} flow of H_2/CO_2/Ar = 6:1:3 at temperatures in the range 220−280 °C for 52 h (C). UiO-67-bipy(N) (D).

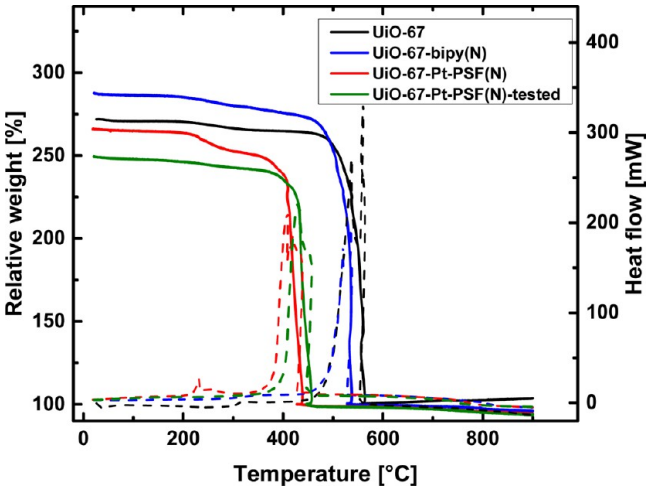

Figure 9. TG curves (solid lines) and differential thermal analysis (DTA) curves (dashed lines) of UiO-67 (black), UiO-67-bipy(N) (blue), and UiO-67-Pt-PSF(N) before (red) and after (green) preactivation in 10% H_2/Ar followed by testing for the CO_2 hydrogenation reaction under a 10−20 mL·min^{-1} flow of H_2/CO_2/Ar = 6:1:3 at temperatures in the range 220−280 °C for 52 h. The samples were heated from 20 to 900 °C at 5 °C·min^{-1} in a flow of synthetic air (20 mL·min^{-1} N_2 and 5 mL·min^{-1} O_2).

was observed. For the sample activated in 10% H_2, the initial conversion was further increased as compared to the 0 and 3% activated samples. It stabilized around 7.5% and was nearly constant throughout the test. The pronounced dependence of the activity on the preactivation atmosphere strongly indicates that the active component of UiO-67-Pt for CO_2 hydrogenation is the Pt NPs formed during activation under a reducing atmosphere. The correlation between Pt metal particle formation and catalytic activity for CO_2 reduction is in agreement with recent literature, which demonstrated a substantial activity difference between supported, individual Pt atoms and Pt metal clusters, respectively, for CO oxidation to CO_2 with either O_2 or H_2O as the oxidizing agent.[33] The observed increase in CO_2 conversion with time on stream, being strongest for the 0% H_2/Ar sample, strongly suggests that migration of Pt entities to form Pt−Pt bonds continues under test conditions.

In the 0% H_2/Ar activated sample, CO was initially the only product formed. However, after 2 h on stream, the selectivity toward CH_4 increased to around 2%. The scattering observed in the selectivity data is presumably due to a CH_4 concentration close to the detection limit, resulting in a high uncertainty. Activation in 3% and 10% H_2/Ar led to a slightly lower CO selectivity (97%) and a correspondingly higher selectivity toward CH_4 (3%), as compared to the inert activated sample. A slight increase in CO selectivity was observed with increasing time on stream, which may suggest that the reaction atmosphere influences the structure of the Pt NPs (*vide infra*).[7] Conversion and selectivity data for the reference catalyst Pt/SiO_2 is also shown in Figure 2. Similar conversion was obtained over this catalyst as over UiO-67-Pt-PSF(M), in spite of higher Pt content and dispersion (Table 1). In contrast to the UiO-67-Pt samples, CO was the only product observed for the CO_2 hydrogenation reaction over Pt/SiO_2. The high CO selectivity of the reaction over Pt/SiO_2 is mainly attributed to a significant destabilization of CO adsorbed on the interface between the support and the Pt NPs through interactions with OH groups on the support.[34] Thus, the shifted product selectivity of the UiO-67-Pt samples toward CH_4 formation hints to a strong metal−support interaction in the Zr-MOF supported catalyst. Previous literature emphasizes the role of the support (Al_2O_3, CeO_2, and TiO_2) and Pt-support interface as a CO_2 activation site.[34−37]

To further investigate the differences between UiO-67-Pt-PSF(N) and Pt/SiO_2, FT-IR measurements were performed. Carbon monoxide is well-known for its strong interaction with d orbitals of transition metals, and its IR spectral features are strongly influenced by the surroundings of its chemisorption sites. For this reason, CO has been extensively employed for the study of metal surfaces (either in the bulk or in the nanoparticle form).[38−43] IR spectra of chemisorbed CO on three samples (Pt/SiO_2 reference, UiO-67-Pt-PSF(N) as activated and after the reaction) are shown in Figure 3. The details for spectra deconvolution are available in the Supporting Information in Figures S5, S6, and S7 and in Tables S2, S3, and S4.

All the samples show the typical spectral features of CO linearly adsorbed on one single Pt atom between 2100 and 1950 cm^{-1} and CO adsorbed on two adjacent Pt atoms (bridged) between 1900 and 1750 cm^{-1}.[44−48] In the former region, it is possible to distinguish two signals: (i) the feature centered around 2050 cm^{-1}, ascribable to carbon monoxide linearly

DOI: 10.1021/acs.iecr.7b01457
Ind. Eng. Chem. Res. 2017, 56, 13206−13218

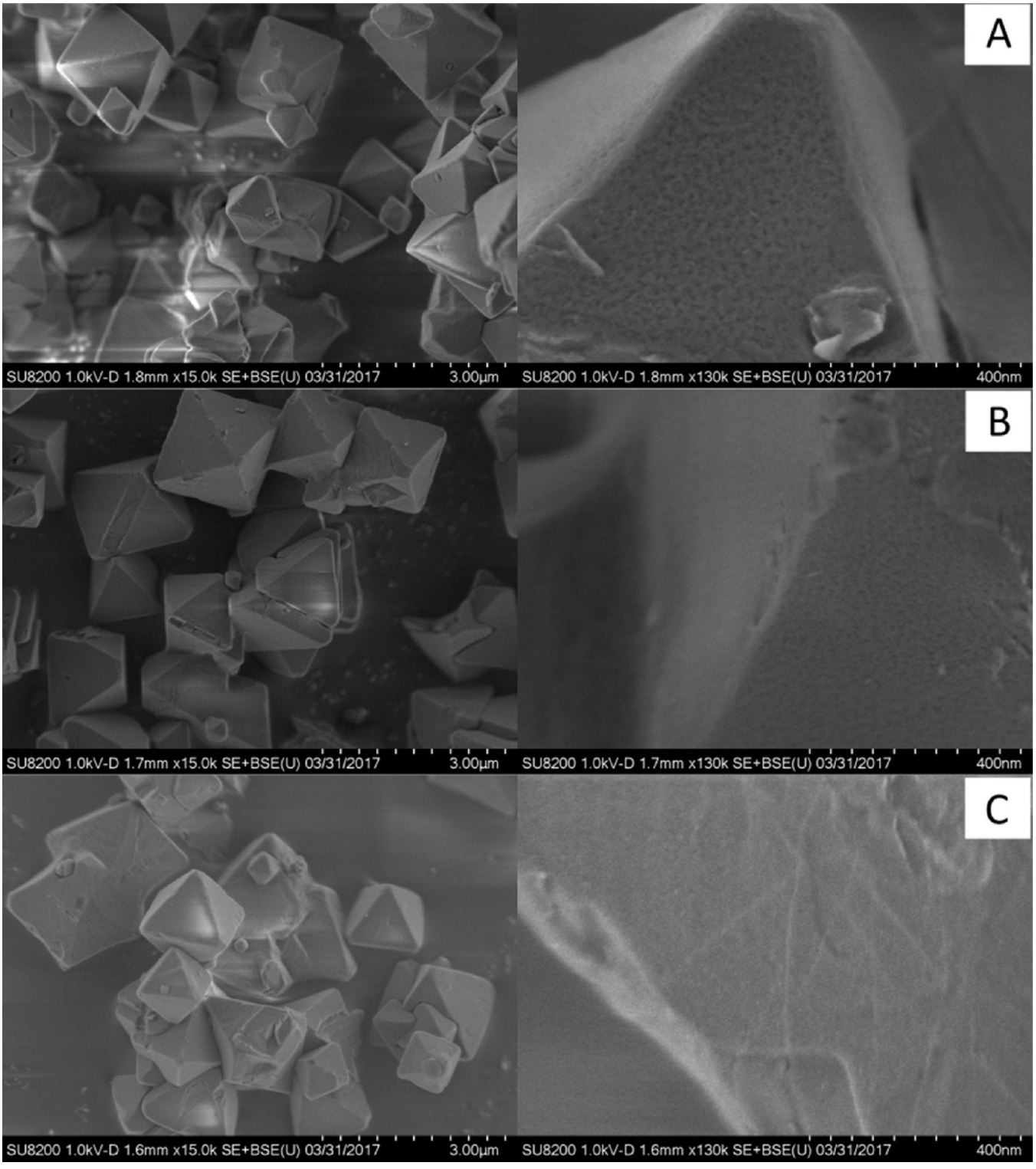

Figure 10. FESEM images of UiO-67-Pt-PSF(N) powder (A), pellets pressed at 0.5 tons (B), and after preactivation in 10% H_2/Ar followed by testing for the CO_2 hydrogenation reaction under a 10−20 mL·min^{-1} flow of H_2/CO_2/Ar = 6:1:3 at temperatures in the range 220−280 °C for 52 h (C). Instrumental magnification: 15 000× (left column) and 130 000× (right column).

adsorbed on the edges of crystalline plains,[44,45,48] and (ii) the peak at 2020−2030 cm^{-1}, related to carbon monoxide linearly adsorbed on the kink positions of Pt nanoparticles.[45,46,48] The position of the peak in the latter region is typical for CO bridged between two atoms at the edges of the particle. For both samples, the features related to CO linearly adsorbed on crystalline faces of the nanoparticles in the region 2100−2070 cm^{-1} are absent.[44−46] We could relate this information with the extremely small dimensions of the particles in both the systems, for which it is not possible to describe a crystalline structure, as evident from the XRD and TEM data (section 3.3.2).

For the MOF catalyst, two additional signals are observed. The first is a small feature around 2120−2110 cm^{-1}, belonging to CO adsorbed on isolated Pt in atomic form, coordinated to the N

DOI: 10.1021/acs.iecr.7b01457
Ind. Eng. Chem. Res. 2017, 56, 13206−13218

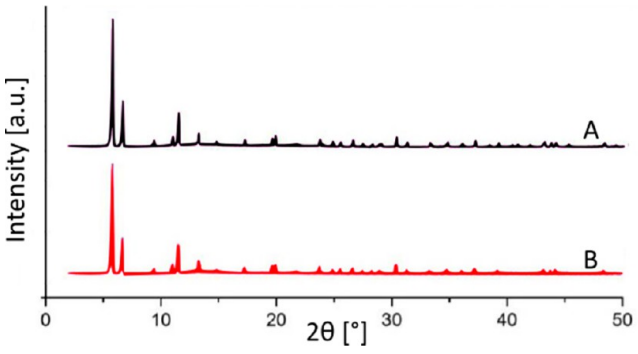

Figure 11. XRD patterns of UiO-67-Pt-PMLS after activation in 10% H_2/Ar (A) and operation under a flow of $H_2/CO_2/Ar$ = 3:1:6 at 250 °C for 16 h (B).

atoms of the bipy ligand.[10,49−51] This kind of site is present due to the incomplete aggregation of Pt into nanoparticles during the preactivation procedure (Figure 1). The second signal is a sharp feature centered at 1720 cm^{-1}, ascribable to CO adsorbed on Pt atoms in close vicinity to the support, and in particular to the aromatic rings of the linkers in UiO-67.[45]

Test results obtained during 52 h on stream for the UiO-67-Pt-PSF(N) sample are shown in Figure 3. An increasing CO_2 conversion as well as CO selectivity was observed with time on stream. The increased conversion is consistent with the observed increase in Pt dispersion after testing (Table 1) and suggests that Pt is further reduced under test conditions. Considering the IR spectra, it is difficult to find clear differences in the active phase UiO-67-Pt-PSF(N) after preactivation, and after long-term operation under reaction conditions, which can justify the changes observed in activity and selectivity during time on stream. One possibility could be a different degree of desorption of CO: it is noticeable that in the sample after H_2 activation, carbon monoxide is adsorbed more strongly compared to the sample after performing the reaction, as suggested by a smaller difference in the total area between the first and last desorption step (Table S3 and S4). This fact could improve the turnover of CO adsorbed on a catalyst's surface, leading to increased activity. However, this observation alone cannot fully explain the changes in activity and selectivity of the MOF-supported catalyst.

3.2.2. Kinetic Investigation. Crystal Size Variation. A major concern with micro- and nanoporous catalysts is the possible influence of diffusion restrictions. To ensure, first, that the test rig was operated under reaction limited conditions, the catalytic activity toward the hydrogenation of CO_2 was measured at various reactor loadings. The results are presented in the Supporting Information, Figure S4, and show that the observed CO_2 conversion rates were not influenced by external or intercrystalline diffusion. To investigate the influence of intracrystalline diffusion, two batches of UiO-67-Pt catalyst with different crystal sizes (UiO-67-Pt-PSF(N) and UiO-67-Pt-PSF(SA)) were prepared and compared. The first batch (UiO-67-Pt-PSF(SA)) had an average crystal size of 0.15 μm, whereas the second batch (UiO-67-Pt-PSF(N)) had an average crystal size of 2 μm (Table 1). Testing of the samples under standard conditions showed that the smaller crystals were less active than the larger crystals (Figure S1). This difference correlates very well with the lower Pt content and similar dispersion of the SA as compared to the N sample (Table 1). More importantly, the catalysts were subjected to temperature variation tests, in order to compare their apparent activation energy for the title reaction. A ln(rate) versus $1/T$ plot comprising both catalysts is shown Figure 4. The apparent activation energy is very similar for the two catalysts in the full temperature range, clearly suggesting that the observed reaction rates are limited by reaction kinetics and not by intracrystalline diffusion.

Contact Time Variation. To elucidate whether CO and CH_4 were formed sequentially or in parallel, the catalyst was subjected to contact time variation experiments in the temperature range 220−280 °C. The yield of CO and CH_4 is plotted as a function of conversion in Figure 5. The selectivity to CO is high (>95%) under all tested conditions, leading to a linear CO yield versus conversion plot which crosses the origin. The CH_4 yield, on the other hand, is low and crosses the abscissa at conversions higher than zero at all temperatures. This result shows that CH_4 is a secondary product formed from CO, suggesting a reverse-water−gas shift (RWGS) reaction followed by a CO methanation pathway.[34] It is interesting to note that the CH_4 yield versus conversion plot crosses the abscissa at higher values with increasing temperature, thereby suggesting that the relative rates of the CO-forming and CO-consuming reactions are shifted toward CH_4 formation at lower temperatures. This shift is not induced by thermodynamics; methane formation is strongly favored in the full temperature range, and the conversion level of the RWGS reaction (eq 1) is further from equilibrium at the lower temperatures.

Having established that the RWGS reaction is the first step in CO_2 hydrogenation under the conditions studied here, it follows

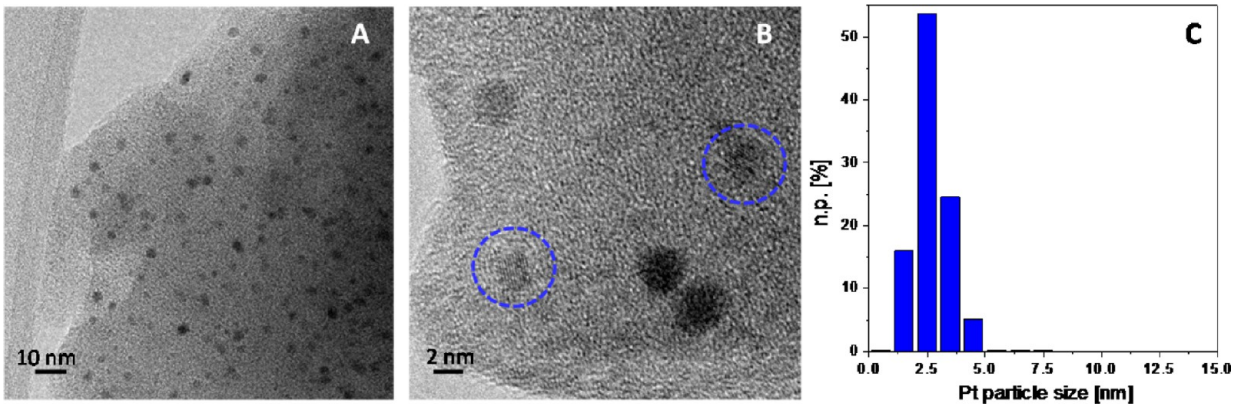

Figure 12. Low magnification (A) and high magnification (B) TEM images of UiO-67-Pt-PMLS after preactivation at 350 °C in a 10% H_2/He flow. Pt particle size distribution (C). Instrumental magnification: 150 000× (A) and 600 000× (B).

DOI: 10.1021/acs.iecr.7b01457
Ind. Eng. Chem. Res. 2017, 56, 13206−13218

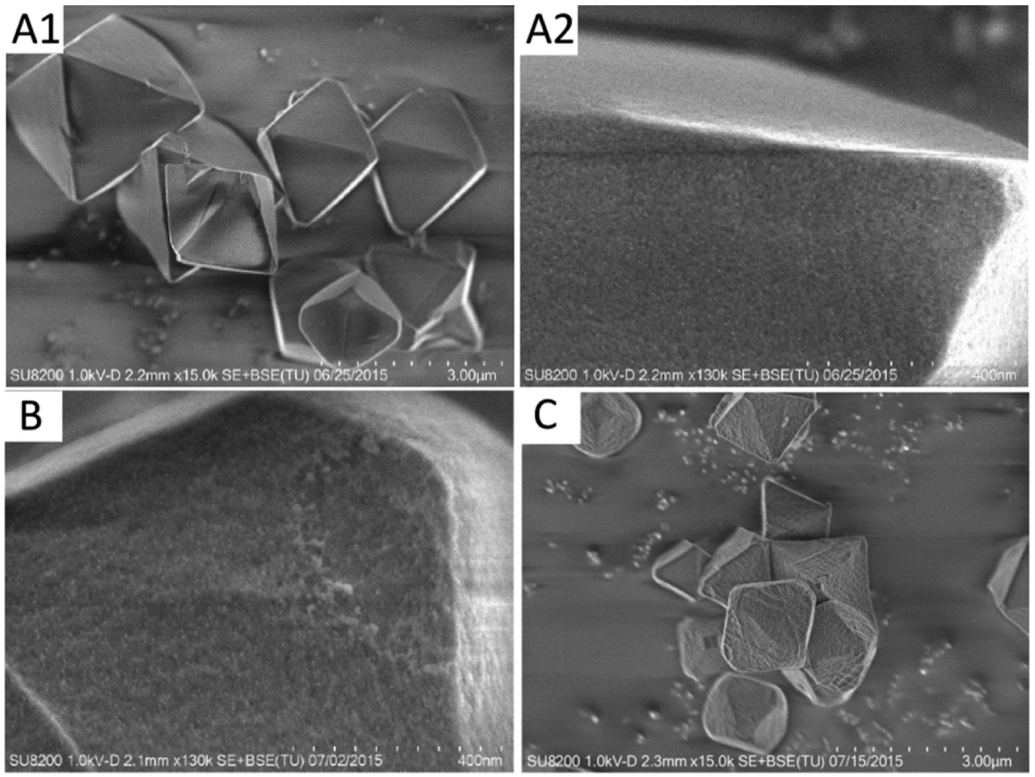

Figure 13. FESEM images of UiO-67-Pt-PMLS after activation in 10% H_2/Ar (A1, A2) and operation under flow of H_2/CO_2/Ar = 3:1:6 at 250 °C for 16 h (B) and for 60 h (C). Instrumental magnification: 15 000× (A1, C) and 130 000× (A2, B).

that CO_2 is initially consumed through a single reaction, a fact that simplifies the following kinetic analysis.

Partial Pressure Variation. The effect of CO_2 partial pressure on the rates of CO and CH_4 formation at 240 and 260 °C is presented in Figure 6. Constant reaction orders with respect to pCO_2 are observed in the entire pressure range (pCO_2 = 0.07−0.4) at each temperature. The reaction orders of CO formation are 0.45 and 0.5 at 240 and 260 °C, respectively, which is lower than the order in CO_2 for the reaction over Pt/TiO_2[37] (0.79 at 350 °C and 3.4 bar) and in good agreement with Pt−Ca/C[52] (0.45 at 220 °C and 1 bar). In oxygen deficient supports, such as Al_2O_3, CeO_2, and TiO_2, CO_2 is adsorbed on either the support[36] or at the interface between Pt and the support, facilitated in both mechanisms by an oxygen vacancy.[34,35] Similarly, on hydroxylated support surfaces (e.g., SiO_2), CO_2 binds at the interface between Pt and the support, stabilized by OH groups.[34] In Pt−Ca/C, the activity—and presumably also the mechanism of reaction—is influenced by Pt−Ca and Ca−CO_2 interactions.[7] As highly similar orders in CO_2 for UiO-67-Pt-PSF(N) and Pt−Ca/C are observed, it may suggest that the interaction between the CO_2 and the catalyst are of a similar nature.

The effect of H_2 partial pressure on the rate of CO and CH_4 formation at 240 and 260 °C is presented in Figure 7. At both temperatures, the reaction order of CO formation with respect to pH_2 is 0.3, which is in good agreement with the 0.25 reported for Pt/TiO_2[37] (at 350 °C and 3.4 bar) and slightly lower than the reported order of 0.46 over Pt−Ca/C.[52] The marginal influence of pH_2 on the rate of CO formation suggests that the catalyst surface is largely covered by hydrogen, readily available for reaction even at a low partial pressure.

Apparent Activation Energy. The apparent activation energy (E_{app}) of CO_2 conversion was elucidated by performing experiments in the temperature range 220−280 °C at constant pCO_2 (0.1 bar), pH_2 (0.6 bar), and τ (0.01 g_{cat}·min·mL^{-1}). The results are presented as an Arrhenius type plot in Figure 4. The E_{app} of CO_2 conversion over all the UiO-67-Pt samples, and the Pt/SiO_2 sample, is calculated to 49−50 kJ·mol^{-1} (Table 2), suggesting that the rate-determining step of CO_2 hydrogenation is the same for all the materials. The lower activity of the Pt/SiO_2 material could be related to lower coverage of reactants or to the larger Pt particles. Considering the difference in CH_4 selectivity over the two materials, the IR measurements suggest that CO is more readily desorbed from the Pt/SiO_2 material, in agreement with the higher abundance of OH groups present on the SiO_2 surface.[34] Such reasoning could also be applied to the negative effect of time on stream and reaction temperature on CH_4 selectivity over the UiO-67-Pt-PSF material: CO was more easily desorbed from the used catalyst (Figure 3), and a lower CO coverage is expected at higher temperature due to entropy effects. However, the results of this study do not preclude a more direct involvement of the UiO-67-bipy framework in the CO_2 hydrogenation reaction.

3.3. Catalyst Stability. *3.3.1. The UiO-67-Pt-PSF(N) Sample.* Figure 8 shows XRD patterns and N_2 adsorption isotherms of the UiO-67-Pt-PSF(N) sample before (A) and after (B) pressing at 0.5 tons, and after preactivation followed by testing for 52 h (C). XRD patterns and N_2 adsorption isotherms of UiO-67-bipy(N) are included for comparison (D). The XRD pattern is fully consistent with the UiO-67 structure. No apparent change in the microcrystalline structure is identified from the XRD patterns after various treatments, suggesting that the lattice of UiO-67-Pt-PSF(N) is stable under the respective conditions. In agreement with the XRD results, only minor differences are observed in the N_2 adsorption isotherms of UiO-67-bipy(N) and UiO-67-Pt-PSF(N) after pressing, preactivation and testing (Table 1, Figure 8). The lattice stability under reaction

DOI: 10.1021/acs.iecr.7b01457
Ind. Eng. Chem. Res. 2017, 56, 13206−13218

conditions is particularly noteworthy, since water is formed in the reaction and UiO-67 has previously been shown to have limited steam stability at room temperature.[12] The reason for the higher stability under reaction conditions could be the lower affinity for water at the reaction temperature (220−280 °C). Literature studies show that, starting at 250 °C, the Zr_6O_6 cluster is reversibly dehydrated by the removal of two H_2O molecules.[16]

Thermogravimetric (TG) measurements obtained during heating of UiO-67, UiO-67-bipy, and UiO-67-Pt-PSF(N) are shown in Figure 9. Similar temperature behavior was observed for the UiO-67 and UiO-67-bipy samples, suggesting that the introduction of 5% bipy linker in the lattice had a minor influence on lattice stability. However, the Pt-containing samples degraded at a lower temperature than the other two samples. This difference probably results from slight changes introduced in the lattice with the grafting of $PtCl_2$ to the bipy linker, which are likely to induce mechanical stress.[53] Pt may also possibly play a more active role as a catalyst of lattice degradation. No significant change in decomposition temperature was observed for the UiO-67-Pt-PSF(N) sample after preactivation in 10% H_2/Ar followed by testing for the CO_2 hydrogenation reaction under a 10−20 mL·min^{-1} flow of $H_2/CO_2/Ar$ = 6:1:3 at temperatures in the range 220−280 °C for 52 h. Thus, Pt-containing UiO-67 exhibits remarkable thermal stability under oxidizing conditions even after thermal treatment at 350 °C under reducing conditions, and long-term testing for the title reaction at temperatures as high as 280 °C.

FESEM images of the UiO-67-Pt-PSF(N) sample are shown in Figure 10, after drying in the air at 150 °C (A), pressing at 0.5 tons (B), and after preactivation in 10% H_2/Ar at 350 °C for 1 h followed by testing for the CO_2 hydrogenation reaction at 220−280 °C for 52 h (C). As a first note, the crystal morphology was maintained during testing, including pressing and sieving prior to testing (see section 2.3). Furthermore, the surface topology was intact after pressing; however, some lines were observed on the crystal surfaces after testing. They could represent scratches from the pressing and sieving treatment or could have been formed during testing. Finally, no Pt particle formation was observed on the outer crystal surface after 52 h of testing, thereby suggesting that the Pt nanoparticles which were formed during the preactivation step (*vide ultra*) were stabilized inside the crystal lattice.

In conclusion, the UiO-67-Pt-PSF(N) sample showed excellent stability under the test conditions used in this study.

3.3.2. The UiO-67-Pt-PMLS Sample. Detailed characterization was also performed for a sample prepared by the PMLS method. In order to follow the lattice stability before and after preactivation and testing by FESEM, it was decided to test it without pressing and sieving it to a given particle size, to avoid mechanical damage of the crystal surface. This means that the flow conditions during catalytic testing were not optimal, and for that reason, the catalytic test data are not reported here. However, UiO-67-Pt-PMLS catalyst performed very similarly to the UiO-67-Pt-PSF(M) catalyst, reported in section 3.2.1 and Supporting Information section S3, with respect to activity, selectivity, and stability.

X-ray diffractograms of the UiO-67-Pt-PMLS sample after preactivation and after testing for 16 h are shown in Figure 11. The diffractograms clearly indicate that the UiO-67-Pt-PMLS lattice is stable under reducing as well as reaction conditions.

TEM images of the UiO-67-Pt-PMLS sample after preactivation at 350 °C in 10% H_2/He flow are shown in Figure 12. The crystallinity of the UiO-67 framework was pointed out by the appearance of diffraction fringes with a spacing of 14 Å (the same spacing as that related to the main diffraction peak in the XRD pattern of the UiO-67-Pt-PMLS sample (Figure 5)) observed at low magnification (A). At the same time, roundish Pt nanoparticles, well contrasted with respect to UiO-67, were clearly detected. Moreover, the analysis at higher magnification (B) put in evidence the presence of crystalline Pt nanoparticles (signaled by blue circles in the figure) with a *d* spacing of 2.25 Å related to the 1 1 1 face of the cubic phase (JCPDS file number 00-001-1194).

The Pt particle size distribution is shown in Figure 3C. Highly dispersed Pt nanoparticles, with an average size of 2.6 ± 0.8 nm, were observed. The particle size distribution is quite narrow, and a large fraction (>50%) of counted nanoparticles has a size of 2.5 nm, strikingly close to the size of the octahedral cavities in the UiO-67 structure (2.3 nm). Despite the high dispersion, these nanoparticles did not coalesce after prolonged time under the electron beam, meaning that they are stabilized within the UiO MOF framework.

FESEM images of the UiO-67-Pt-PMLS sample are shown in Figure 13, after preactivation in 10% H_2/He at 350 °C for 1 h (A1, A2) and after testing for the CO_2 hydrogenation reaction at 250 °C for 16 h (B) and 60 h (C). As a first note, comparison between Figure 13A1 and C suggests that the crystal morphology was maintained during preactivation and testing. Furthermore, the surface topology seemed intact after preactivation and testing for 16 h. A slight roughening of the crystal surfaces could be suggested from the lower resolution FESEM image of the sample tested for 60 h, but a close-up image revealed no damage of the surface. Finally, no Pt particle formation was observed on the outer crystal surface after any of the treatments, thereby suggesting that the Pt nanoparticles which were formed during the preactivation step (Figure 12) were stabilized inside the crystal lattice, in agreement with the TEM findings. In conclusion, the PMLS synthesis procedure yielded a material with excellent stability under CO_2 hydrogenation conditions, in line with the PSF method.

4. CONCLUSION

In this work, Pt was introduced to the UiO-67 Zr-MOF framework by grafting it to a bipyridine-based linker, which constituted 5% of the framework linkers. Pt nanocrystals were obtained by preactivation in flowing H_2/Ar at 350 °C. Thorough characterization of as-made, preactivated, and tested material (T = 220−280 °C and ambient pressure, with H_2/CO_2 ratios in the range 0.2−9 and contact times in the range 0.004−0.01 g_{cat}·min·mL^{-1} for up to 60 h) showed that the UiO-67 Zr-MOF framework was stable during all treatments.

Catalytic testing for the CO_2 hydrogenation reaction showed that CO_2 conversion is positively correlated with the degree of Pt reduction, in accordance with recent literature. CO selectivity above 90% was obtained under all tested conditions. Contact time variation experiments showed that CO is a primary product of reaction, while CH_4 is a secondary product, formed via CO. A low reaction order in pH_2 and pCO_2 was observed, suggesting high coverage of the active site(s). Testing of catalyst crystals with 0.15 and 2.0 μm crystal size, respectively, revealed no influence of diffusion on the reaction rate. Comparison to a conventional Pt/SiO_2 catalyst showed very similar activation energy, with E_{app} = 50 ± 3 kJ·mol^{-1} suggesting that CO_2 hydrogenation follows the same mechanism over the two materials.

DOI: 10.1021/acs.iecr.7b01457
Ind. Eng. Chem. Res. 2017, 56, 13206−13218

Overall, this study shows that the partially bipy-functionalized UiO-67 Zr-MOF framework is well suited as a support for the Pt-catalyzed reverse-water−gas shift reaction and is able to stabilize Pt metal nanoparticles of a similar size to the framework cavities. Comparison to a conventional Pt/SiO_2 catalyst further demonstrated that the Zr-MOF framework facilitated hydrogenation of CO to CH_4. Future introduction of a second functionality in the Zr-MOF material, aimed at the stabilization of Pt-CO entities, is expected to further promote this reaction.

■ ASSOCIATED CONTENT

Supporting Information

The Supporting Information is available free of charge on the ACS Publications website at DOI: 10.1021/acs.iecr.7b01457.

Catalytic performance of UiO-67-Pt-PSF during long-term testing and reuse, characterization of UiO-67-Pt-PSF(M) (N_2 adsorption and XRD), tests of diffusion influence, detailed material synthesis, deconvolution of FT-IR spectra, and FESEM of Pt/SiO_2 (PDF)

■ AUTHOR INFORMATION

Corresponding Author

*E-mail: unni.olsbye@kjemi.uio.no.

ORCID

Andrea Lazzarini: 0000-0002-0404-6597
Elisa Borfecchia: 0000-0001-8374-8329
Carlo Lamberti: 0000-0001-8004-2312
Silvia Bordiga: 0000-0003-2371-4156
Bert M. Weckhuysen: 0000-0001-5245-1426
Unni Olsbye: 0000-0003-3693-2857

Present Address

#M.M.: Department of Drug Science and Technology and NIS Interdepartmental Centre, University of Turin, 10125 Torino, Italy

Notes

The authors declare the following competing financial interest(s): U.O. and K.P.L. are co-founders of ProfMOF A/S, a company targeting scale-up of MOF materials.

■ ACKNOWLEDGMENTS

E.S.G., S.Ø.-Ø., A.L., S.A., B.B., B.T.L.-B., R.H., K.P.L., and U.O. acknowledge the Norwegian Research Council for financial support through contracts 215735, 228157, and 250795. C.L. and L.B. acknowledge the founding from the Mega-Grant of Ministry of Education and Science of the Russian Federation (14.Y26.31.0001). E.B. acknowledges Innovation Fund Denmark (Industrial postdoc no. 5190-00018B). B.M.W. acknowledges financial support from a Netherlands Organization of Scientific Research (NWO) Gravitation program (Netherlands Center for Multiscale Catalytic Energy Conversion, MCEC) as well as a European Research Council (ERC) Advanced Grant (no. 321140). We are grateful to MAX-lab for the allocation of beam time (proposal 20140449) and to Dr. Stefan Carlson for technical support during the experiments at the I811 beamline.

■ REFERENCES

(1) Jiang, Z.; Xiao, T.; Kuznetsov, V. L.; Edwards, P. P. Turning carbon dioxide into fuel. *Philos. Trans. R. Soc., A* **2010**, *368*, 3343−3364.

(2) Chen, Z.; Deutsch, T. G.; Dinh, H. N.; Domen, K.; Emery, K.; Forman, A. J.; Gaillard, N.; Garland, R.; Heske, C.; Jaramillo, T. F.; Kleiman-Shwarsctein, A.; Miller, E.; Takanabe, K.; Turner, J. UV-Vis Spectroscopy. In *Photoelectrochemical Water Splitting: Standards, Experimental Methods, and Protocols*; Springer: New York, 2013; pp 49−62.

(3) Wang, W.; Wang, S.; Ma, X.; Gong, J. Recent advances in catalytic hydrogenation of carbon dioxide. *Chem. Soc. Rev.* **2011**, *40*, 3703−3727.

(4) Westermann, A.; Azambre, B.; Bacariza, M. C.; Graça, I.; Ribeiro, M. F.; Lopes, J. M.; Henriques, C. Insight into CO_2 methanation mechanism over NiUSY zeolites: An operando IR study. *Appl. Catal., B* **2015**, *174*−*175*, 120−125.

(5) Aldana, P. A. U.; Ocampo, F.; Kobl, K.; Louis, B.; Thibault-Starzyk, F.; Daturi, M.; Bazin, P.; Thomas, S.; Roger, A. C. Catalytic CO_2 valorization into CH_4 on Ni-based ceria-zirconia. Reaction mechanism by operando IR spectroscopy. *Catal. Today* **2013**, *215*, 201−207.

(6) Gao, J.; Liu, Q.; Gu, F.; Liu, B.; Zhong, Z.; Su, F. Recent advances in methanation catalysts for the production of synthetic natural gas. *RSC Adv.* **2015**, *5*, 22759−22776.

(7) Román-Martínez, M. C.; Cazorla-Amorós, D.; Salinas-Martínez de Lecea, C.; Linares-Solano, A. Structure Sensitivity of CO_2 Hydrogenation Reaction Catalyzed by Pt/Carbon Catalysts. *Langmuir* **1996**, *12*, 379−385.

(8) Wei, J.; Iglesia, E. Mechanism and Site Requirements for Activation and Chemical Conversion of Methane on Supported Pt Clusters and Turnover Rate Comparisons among Noble Metals. *J. Phys. Chem. B* **2004**, *108*, 4094−4103.

(9) Sumida, K.; Rogow, D. L.; Mason, J. A.; McDonald, T. M.; Bloch, E. D.; Herm, Z. R.; Bae, T.-H.; Long, J. R. Carbon Dioxide Capture in Metal−Organic Frameworks. *Chem. Rev.* **2012**, *112*, 724−781.

(10) Øien, S.; Agostini, G.; Svelle, S.; Borfecchia, E.; Lomachenko, K. A.; Mino, L.; Gallo, E.; Bordiga, S.; Olsbye, U.; Lillerud, K. P.; Lamberti, C. Probing Reactive Platinum Sites in UiO-67 Zirconium Metal−Organic Frameworks. *Chem. Mater.* **2015**, *27*, 1042−1056.

(11) Huang, H.; Zhang, W.; Yang, F.; Wang, B.; Yang, Q.; Xie, Y.; Zhong, C.; Li, J.-R. Enhancing CO_2 adsorption and separation ability of Zr(IV)-based metal−organic frameworks through ligand functionalization under the guidance of the quantitative structure−property relationship model. *Chem. Eng. J.* **2016**, *289*, 247−253.

(12) Øien-Ødegaard, S.; Bouchevreau, B.; Hylland, K.; Wu, L.; Blom, R.; Grande, C.; Olsbye, U.; Tilset, M.; Lillerud, K. P. UiO-67-type Metal−Organic Frameworks with Enhanced Water Stability and Methane Adsorption Capacity. *Inorg. Chem.* **2016**, *55*, 1986−1991.

(13) Wang, B.; Huang, H.; Lv, X.-L.; Xie, Y.; Li, M.; Li, J.-R. Tuning CO_2 Selective Adsorption over N_2 and CH_4 in UiO-67 Analogues through Ligand Functionalization. *Inorg. Chem.* **2014**, *53*, 9254−9259.

(14) Wang, C.; Xie, Z.; deKrafft, K. E.; Lin, W. Doping Metal−Organic Frameworks for Water Oxidation, Carbon Dioxide Reduction, and Organic Photocatalysis. *J. Am. Chem. Soc.* **2011**, *133*, 13445−13454.

(15) Katz, M. J.; Brown, Z. J.; Colon, Y. J.; Siu, P. W.; Scheidt, K. A.; Snurr, R. Q.; Hupp, J. T.; Farha, O. K. A facile synthesis of UiO-66, UiO-67 and their derivatives. *Chem. Commun.* **2013**, *49*, 9449−9451.

(16) Cavka, J. H.; Jakobsen, S.; Olsbye, U.; Guillou, N.; Lamberti, C.; Bordiga, S.; Lillerud, K. P. A New Zirconium Inorganic Building Brick Forming Metal Organic Frameworks with Exceptional Stability. *J. Am. Chem. Soc.* **2008**, *130*, 13850−13851.

(17) Rimoldi, M.; Howarth, A. J.; DeStefano, M. R.; Lin, L.; Goswami, S.; Li, P.; Hupp, J. T.; Farha, O. K. Catalytic Zirconium/Hafnium-Based Metal−Organic Frameworks. *ACS Catal.* **2017**, *7*, 997−1014.

(18) Vermoortele, F.; Vandichel, M.; Van de Voorde, B.; Ameloot, R.; Waroquier, M.; Van Speybroeck, V.; De Vos, D. E. Electronic Effects of Linker Substitution on Lewis Acid Catalysis with Metal−Organic Frameworks. *Angew. Chem., Int. Ed.* **2012**, *51*, 4887−4890.

(19) Liu, Y.; Klet, R. C.; Hupp, J. T.; Farha, O. Probing the correlations between the defects in metal-organic frameworks and their catalytic activity by an epoxide ring-opening reaction. *Chem. Commun.* **2016**, *52*, 7806−7809.

(20) Toyao, T.; Miyahara, K.; Fujiwaki, M.; Kim, T.-H.; Dohshi, S.; Horiuchi, Y.; Matsuoka, M. Immobilization of Cu Complex into Zr-Based MOF with Bipyridine Units for Heterogeneous Selective Oxidation. *J. Phys. Chem. C* **2015**, *119*, 8131−8137.

DOI: 10.1021/acs.iecr.7b01457
Ind. Eng. Chem. Res. 2017, 56, 13206−13218

(21) Li, X.; Guo, Z.; Xiao, C.; Goh, T. W.; Tesfagaber, D.; Huang, W. Tandem Catalysis by Palladium Nanoclusters Encapsulated in Metal−Organic Frameworks. *ACS Catal.* **2014**, *4*, 3490−3497.
(22) An, B.; Zhang, J.; Cheng, K.; Ji, P.; Wang, C.; Lin, W. Confinement of Ultrasmall Cu/ZnOx Nanoparticles in Metal−Organic Frameworks for Selective Methanol Synthesis from Catalytic Hydrogenation of CO_2. *J. Am. Chem. Soc.* **2017**, *139*, 3834−3840.
(23) Guo, Z.; Xiao, C.; Maligal-Ganesh, R. V.; Zhou, L.; Goh, T. W.; Li, X.; Tesfagaber, D.; Thiel, A.; Huang, W. Pt Nanoclusters Confined within Metal−Organic Framework Cavities for Chemoselective Cinnamaldehyde Hydrogenation. *ACS Catal.* **2014**, *4*, 1340−1348.
(24) Choi, K. M.; Na, K.; Somorjai, G. A.; Yaghi, O. M. Chemical environment control and enhanced catalytic performance of platinum nanoparticles embedded in nanocrystalline metal−organic frameworks. *J. Am. Chem. Soc.* **2015**, *137*, 7810−7816.
(25) Hester, P.; Xu, S.; Liang, W.; Al-Janabi, N.; Vakili, R.; Hill, P.; Muryn, C. A.; Chen, X.; Martin, P. A.; Fan, X. On thermal stability and catalytic reactivity of Zr-based metal−organic framework (UiO-67) encapsulated Pt catalysts. *J. Catal.* **2016**, *340*, 85−94.
(26) Zhuang, G.-l.; Bai, J.-q.; Zhou, X.; Gao, Y.-f.; Huang, H.-l.; Cui, H.-q.; Zhong, X.; Zhong, C.-L.; Wang, J.-g. The Effect of N-Containing Supports on Catalytic CO Oxidation Activity over Highly Dispersed Pt/UiO-67. *Eur. J. Inorg. Chem.* **2017**, *2017*, 172−178.
(27) Freel, J. Chemisorption on supported platinum. *J. Catal.* **1972**, *25*, 139−148.
(28) Haneda, M.; Watanabe, T.; Kamiuchi, N.; Ozawa, M. Effect of platinum dispersion on the catalytic activity of Pt/Al_2O_3 for the oxidation of carbon monoxide and propene. *Appl. Catal., B* **2013**, *142−143*, 8−14.
(29) Valenzano, L.; Civalleri, B.; Chavan, S.; Bordiga, S.; Nilsen, M. H.; Jakobsen, S.; Lillerud, K. P.; Lamberti, C. Disclosing the Complex Structure of UiO-66 Metal Organic Framework: A Synergic Combination of Experiment and Theory. *Chem. Mater.* **2011**, *23*, 1700−1718.
(30) Shearer, G. C.; Forselv, S.; Chavan, S.; Bordiga, S.; Mathisen, K.; Bjørgen, M.; Svelle, S.; Lillerud, K. P. In Situ Infrared Spectroscopic and Gravimetric Characterisation of the Solvent Removal and Dehydroxylation of the Metal Organic Frameworks UiO-66 and UiO-67. *Top. Catal.* **2013**, *56*, 770−782.
(31) Råberg, L. B.; Jensen, M. B.; Olsbye, U.; Daniel, C.; Haag, S.; Mirodatos, C.; Sjåstad, A. O. Propane dry reforming to synthesis gas over Ni-based catalysts: Influence of support and operating parameters on catalyst activity and stability. *J. Catal.* **2007**, *249*, 250−260.
(32) Braglia, L.; Borfecchia, E.; Lomachenko, K. A.; Bugaev, A. L.; Guda, A. A.; Soldatov, A. V.; Bleken, B. T. L.; Oien-Odegaard, S.; Olsbye, U.; Lillerud, K. P.; Bordiga, S.; Agostini, G.; Manzoli, M.; Lamberti, C. Tuning Pt and Cu sites population inside functionalized UiO-67 MOF by controlling activation conditions. *Faraday Discuss.* **2017**, DOI: 10.1039/C7FD00024C.
(33) Ding, K.; Gulec, A.; Johnson, A. M.; Schweitzer, N. M.; Stucky, G. D.; Marks, L. D.; Stair, P. C. Identification of active sites in CO oxidation and water-gas shift over supported Pt catalysts. *Science* **2015**, *350*, 189−192.
(34) Kattel, S.; Yan, B.; Chen, J. G.; Liu, P. CO_2 hydrogenation on Pt, Pt/SiO_2 and Pt/TiO_2: Importance of synergy between Pt and oxide support. *J. Catal.* **2016**, *343*, 115−126.
(35) Ferri, D.; Burgi, T.; Baiker, A. Probing boundary sites on a Pt/Al_2O_3 model catalyst by CO_2 hydrogenation and in situ ATR-IR spectroscopy of catalytic solid-liquid interfaces. *Phys. Chem. Chem. Phys.* **2002**, *4*, 2667−2672.
(36) Goguet, A.; Meunier, F. C.; Tibiletti, D.; Breen, J. P.; Burch, R. Spectrokinetic investigation of reverse water-gas-shift reaction intermediates over a Pt/CeO_2 catalyst. *J. Phys. Chem. B* **2004**, *108*, 20240−20246.
(37) Kim, S. S.; Lee, H. H.; Hong, S. C. A study on the effect of support's reducibility on the reverse water-gas shift reaction over Pt catalysts. *Appl. Catal., A* **2012**, *423*, 100−107.
(38) Crossley, A.; King, D. A. Infrared spectra for CO isotopes chemisorbed on Pt {111}: Evidence for strong absorbate coupling interactions. *Surf. Sci.* **1977**, *68*, 528−538.
(39) Hayden, B. E.; Kretzschmar, K.; Bradshaw, A. M.; Greenler, R. G. An infrared study of the adsorption of CO on a stepped platinum surface. *Surf. Sci.* **1985**, *149*, 394−406.
(40) Heyden, B. E.; Bradshaw, A. M. The adsorption of CO on Pt(111) studied by infrared reflection—Absortion spectroscopy. *Surf. Sci.* **1983**, *125*, 787−802.
(41) Hoffmann, F. M.; Bradshaw, A. M. IR reflection-absorption spectroscopy of CO adsorbed on platinum and palladium. *J. Catal.* **1976**, *44*, 328−331.
(42) Krebs, H.-J.; Lüth, H. Evidence for two different adsorption sites of CO on Pt(111) from infrared reflection spectroscopy. *Appl. Phys.* **1977**, *14*, 337−342.
(43) Shigeishi, R. A.; King, D. A. Chemisorption of carbon monoxide on platinum {111}: Reflection-absorption infrared spectroscopy. *Surf. Sci.* **1976**, *58*, 379−396.
(44) Brandt, R. K.; Hughes, M. R.; Bourget, L. P.; Truszkowska, K.; Greenler, R. G. The interpretation of CO adsorbed on Pt/SiO_2 of two different particle-size distributions. *Surf. Sci.* **1993**, *286*, 15−25.
(45) Cheah, S. K.; Bernardet, V. P.; Franco, A. A.; Lemaire, O.; Gelin, P. Study of CO and Hydrogen Interactions on Carbon-Supported Pt Nanoparticles by Quadrupole Mass Spectrometry and Operando Diffuse Reflectance FTIR Spectroscopy. *J. Phys. Chem. C* **2013**, *117*, 22756−22767.
(46) Coloma, F.; Coronado, J. M.; Rochester, C. H.; Anderson, J. A. Infrared study of crotonaldehyde and CO adsorption on a Pt/TiO_2 catalyst. *Catal. Lett.* **1998**, *51*, 155−162.
(47) Haaland, D. M. Infrared studies of CO adsorbed on Pt/Al_2O_3: Evidence for CO bonded in 3-fold coordination. *Surf. Sci.* **1987**, *185*, 1−14.
(48) Raskó, J. CO-induced surface structural changes of Pt on oxide-supported Pt catalysts studied by DRIFTS. *J. Catal.* **2003**, *217*, 478−486.
(49) Chakarova, K.; Mihaylov, M.; Hadjiivanov, K. FTIR spectroscopic study of CO adsorption on Pt−H−ZSM-5. *Microporous Mesoporous Mater.* **2005**, *81*, 305−312.
(50) Chakarova, K.; Mihaylov, M.; Hadjiivanov, K. Polycarbonyl species in Pt/H−ZSM-5: FTIR spectroscopic study of $^{12}CO-^{13}CO$ co-adsorption. *Catal. Commun.* **2005**, *6*, 466−471.
(51) Kubanek, P.; Schmidt, H. W.; Spliethoff, B.; Schüth, F. Parallel IR spectroscopic characterization of CO chemisorption on Pt loaded zeolites. *Microporous Mesoporous Mater.* **2005**, *77*, 89−96.
(52) Román-Martínez, M. C.; Cazorla-Amoròs, D.; Linares-Solano, A.; Salinas-Martínez de Lecea, C. CO_2 hydrogenation under pressure on catalysts Pt−Ca/C. *Appl. Catal., A* **1996**, *134*, 159−167.
(53) Gonzalez, M. I.; Bloch, E. D.; Mason, J. A.; Teat, S. J.; Long, J. R. Single-Crystal-to-Single-Crystal Metalation of a Metal−Organic Framework: A Route toward Structurally Well-Defined Catalysts. *Inorg. Chem.* **2015**, *54*, 2995−3005.

DOI: 10.1021/acs.iecr.7b01457
Ind. Eng. Chem. Res. 2017, 56, 13206−13218